Exp Fluids (2012) 52:425–440
DOI 10.1007/s00348-011-1227-7

RESEARCH ARTICLE

# Assessment of tomographic PIV in wall-bounded turbulence using direct numerical simulation data

**C. M. de Silva · R. Baidya · M. Khashehchi · I. Marusic**

Received: 3 March 2011 / Revised: 9 October 2011 / Accepted: 7 November 2011 / Published online: 27 November 2011


**Abstract** Simulations of tomographic particle image velocimetry (Tomo-PIV) are performed using direct numerical simulation data of a channel flow at Reynolds number of $Re_\tau = 934$, to investigate the influence of experimental parameters such as camera position, seeding density, interrogation volume size and spatial resolution. The simulations employ camera modelling, a Mie scattering illumination model, lens distortion effects and calibration to realistically model a tomographic experiment. Results are presented for camera position and orientation in three-dimensional space, to obtain an optimal reconstruction quality. Furthermore, a quantitative analysis is performed on the accuracy of first and second order flow statistics, at various voxel sizes normalised using the viscous inner length scale. This enables the result to be used as a general reference for wall-bounded turbulent experiments. In addition, a ratio relating seeding density and the interrogation volume size is proposed to obtain an optimal reference value that remains constant. This can be used to determine the required seeding density concentration for a certain interrogation volume size.

## 1 Introduction

The ability to accurately measure the three-dimensional structure of turbulent flows is of great interest in fluid mechanics as it helps to reveal the topology of turbulent flows, which can be used to validate numerical simulations and provide fundamental insights into the nature of these flows. Particle image velocimetry (PIV) is a measurement technique that has emerged in the past two decades and is considered to be still under development. It is widely used as a measurement technique for complex flow studies with an increasing number of industrial applications. Moreover, studies using two-dimensional PIV (Adrian 1991), stereoscopic PIV (Arroyo and Greated 1991) have shown the capability of the PIV technique to quantitatively visualise complex flows. Recent advancements include three-dimensional versions of the technique, including holographic PIV (HPIV) (Hinsch 2002), scanning PIV (Hori and Sakakibara 2004), particle tracking velocimetry (PTV) (Maas et al. 2004) and synthetic aperture PIV (Belden et al. 2010), which have developed over the last decade.

Tomographic particle image velocimetry (Tomo-PIV) (Elsinga et al. 2006) is a technique for three-component three-dimensional (3C–3D) velocity measurement based on the tomographic reconstruction of an intensity field representing a volume from multiple view points. Tomo-PIV has several advantages over other three-dimensional PIV techniques. For example, it avoids problems of HPIV such as a single line of sight and complex experimental setups. In addition, techniques such as PTV are limited to low seeding densities, yielding low spatial resolution in comparison with Tomo-PIV (Worth and Nickels 2008).

The accuracy of a tomographic approach to PIV is highly dependent on the algorithms used for reconstruction and cross-correlation. Elsinga et al. (2006) suggested the discretisation of the measurement volume into a 3D array of cubic voxel elements to perform a three-dimensional reconstruction. The intensity at each voxel can then be determined iteratively using a multiplicative algebraic

C. M. de Silva · R. Baidya · M. Khashehchi · I. Marusic (✉)
Department of Mechanical Engineering,
University of Melbourne, Melbourne,
VIC, Australia
e-mail: imarusic@unimelb.edu.au

C. M. de Silva
e-mail: c.desilva3@pgrad.unimelb.edu.au

reconstruction technique (MART). This method is further accelerated by improving the initialisation of the volume intensity distribution as suggested by Worth and Nickels (2008). More recent advances on this technique include a multiplicative line-of-sight reconstruction technique (MLOS-SMART) presented by Atkinson and Soria (2009), which considerably reduces reconstruction time by eliminating the iterative procedure. Three-dimensional cross-correlation techniques used in this simulation study is an extension of the two-dimensional cross-correlation techniques that are described in detail by Scarano (2001) and is not reviewed here.

In addition to these algorithms, the accuracy of Tomo-PIV is also highly influenced by several experimental parameters which are analysed in this study. These experimental parameters include the position and orientation of each camera, the number of particles per interrogation volume, seeding particle size and voxel to pixel ratio. To perform this analysis, several simulations were carried out emulating a Tomo-PIV experiment on wall-bounded turbulence. The novelty of the approach presented herein is the application of channel flow direct numerical simulation (DNS) data at $Re_\tau = 934$ (del Alamo et al. 2004) to displace the synthetic particles, providing a realistic vector flow field for such a turbulent flow with large wall-normal heterogeneity. In comparison, Worth et al. (2010) performed a resolution study on Tomo-PIV based on homogenous isotropic turbulence DNS data. Other studies presented by Lecordier and Westerweel (2008) used a constant displacement for all particles.

In this paper, we use the coordinate system $x$, $y$ and $z$ to refer to the streamwise, spanwise and wall-normal directions, respectively, and $U$, $V$ and $W$ describe the respective velocity components. In addition, we use the superscript $+$ to refer to normalisation with the viscous inner scale. For example, $l^+ = lU_\tau/\nu$ and $U^+ = U/U_\tau$, where $U_\tau$ is the friction velocity and $\nu$ is the kinematic viscosity of the fluid. This study focuses on key experimental parameters that have been identified to significantly affect the overall accuracy and have not been studied extensively in existing literature. These parameters are discussed in detail below.

### 1.1 Volume discretisation

The optics, resolution and position of the camera dictates the achievable voxel size $l_v^+$ in the reconstruction procedure. A higher-resolution camera would have a larger number of pixels on its sensor and will capture greater detail with a smaller $l_v^+$ achieving better results. However, higher-resolution cameras have drawbacks, one being that they are more expensive and tend to have lower frame rates. Similarly, a lens that provides a smaller $l_v^+$ has a reduced field of view. In this study, a quantitative analysis on the Tomo-PIV accuracy at varying volume discretisation levels is performed. In addition, we determine the effectiveness of Tomo-PIV to resolve turbulent statistics at varying wall normal height in comparison with DNS.

### 1.2 Particles per interrogation volume ($N_I$) and seeding density

A key decision in any PIV experiment is the seeding density of particles, which influences the accuracy of the three-dimensional cross-correlation. The seeding density directly influences the particles per interrogation volume ($N_I$) (Adrian 1991). This parameter represents the average number of particles in an interrogation volume, which is typically of the size $32 \times 32 \times 32$ or $64 \times 64 \times 64$ voxels depending on the volume discretisation level. If the $N_I$ is low, the cross-correlation will be unable to determine the displacement of each interrogation volume, as it is difficult to obtain a clear peak in the cross-correlation coefficients, and instead several peaks of smaller magnitude are typically detected. Conversely, if the $N_I$ is high, the accuracy is again reduced as there is an increase in ghost particles, and this leads to a higher level of noise in the reconstructed volume. In addition, particles will impede the line-of-sight of other particles from the camera. These factors tend to reduce the peak detection accuracy in the cross-correlation phase. The interrogation volume size can also be changed to reduce or increase the $N_I$ for a given seeding density, thereby affecting the accuracy in detecting a peak. Therefore, it is evident that there is an optimal ratio between seeding density and the interrogation volume size. To analyse this, simulations are run varying the number of synthetic particles (seeding density) and the interrogation volume size.

### 1.3 Camera position and orientation

The position and orientation of the cameras can significantly influence the accuracy of a tomographic reconstruction and thereby lead to a poor cross-correlation. Studies have been performed previously by Elsinga et al. (2006) to determine the influence of the angle between the laser sheet and the camera position; however, these studies were performed by projecting a one-dimensional image to a two-dimensional array of pixels. In this study, we aim to simulate the effect of moving each camera in three-dimensional space by adjusting each camera's azimuthal ($\theta$) and elevation ($\phi$) angles, as shown in Fig. 1. In addition, we model the illumination of a laser light enabling us to determine the influence of positioning cameras in forward and backward scatter in relation to the direction of illumination.

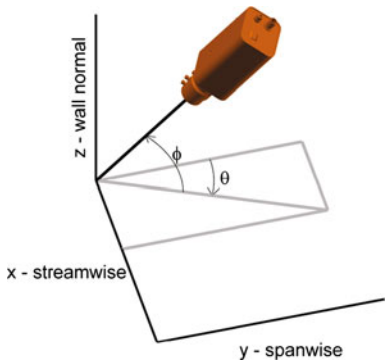


**Fig. 1** Parameters for camera placement. The elevation angle is $\phi$ and $\theta$ is the azimuthal angle

## 2 Methodology

The simulation performed in this analysis has three main components; a calibration process, a reconstruction and a three-dimensional cross-correlation. Simulations were performed in a matrix laboratory computing environment (MATLAB), and using C code for computationally intensive iterative calculations together with a Graphical Processing Unit (GPU). This combination enables a considerable reduction in processing time due to the use of a parallel computational architecture.

### 2.1 Calibration

Tomographic PIV post processing uses a mathematical function $f(x, y, z)$ that maps the three-dimensional volume $(x, y, z)$ to camera coordinates $(X, Y)$. This accounts for inaccuracies arising from perspective distortion and camera misalignment. This function typically takes the form of a second- or third-order polynomial which can be expressed as

$$X = a_1 + a_2x + a_3y + a_4z + \cdots \quad (1)$$

$$Y = b_1 + b_2x + b_3y + b_4z + \cdots \quad (2)$$

where $a_{1,2,3,4,\ldots}, b_{1,2,3,4,\ldots}$ are the polynomial coefficients. In this study, we implemented a third-order polynomial function for the calibration procedure. In previous studies by Elsinga et al. (2006), the reconstruction procedure was done by direct back-projection from the position and orientation of each camera. However, a calibration procedure is required for reconstruction in experimental conditions due to inaccuracies stated previously. Therefore, we model the calibration procedure in our simulations to provide an enhanced assessment of the Tomo-PIV technique and its limitations compared with Elsinga et al. (2006); Lecordier and Westerweel (2008). Furthermore, this enables us to determine the accuracy of different calibration functions and techniques together with the computational time associated at the reconstruction phase.

To determine the calibration coefficients from Eqs. 1 and 2, a synthetic calibration target as shown in Fig. 2 is used with markers placed at known positions, within the volume of interest. The calibration target is then captured from the required camera positions and orientation, thereby emulating the calibration procedure. These images are then processed using an object-detection algorithm which can determine the position of every marker on the calibration target. These marker positions are consequently mapped to its corresponding physical locations within the synthetic volume using the three reference points. Finally, a least square error curve fit is used to determine the corresponding calibration coefficients for the polynomial used.

### 2.2 Synthetic imaging

The next phase involves the generation of a synthetic volume seeded with particles. This is achieved by randomly placing spherical objects within a defined volume based on simulation parameters such as the number and diameter of the particles. The synthetic volume is represented as a figure in the MATLAB environment instead of generating an intensity matrix to define the synthetic volume as used by Elsinga et al. (2006). This enables us to utilise the camera toolbox in MATLAB to capture a synthetic image at the desired discretisation level. In addition, we are able to simulate inaccuracies such as perspective distortion within the synthetic volume. The region occupied by the synthetic volume is considered to be in focus, and this is typically achieved in Tomo-PIV experiments by the use of a Scheimpflug adapters. The cameras are modelled with an 8-bit dynamic range which is typical of PIV cameras.

The lighting scheme in each simulation uses a twofold procedure to model the illumination of the synthetic particles accurately. Firstly, a Phong reflection model (Phong

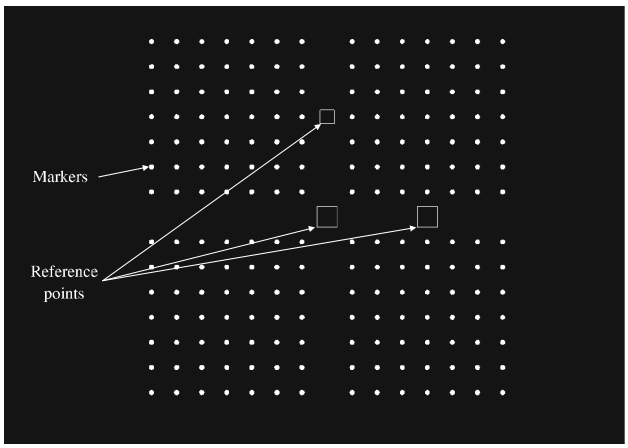


**Fig. 2** Calibration target used in the calibration procedure

1975) is used to illuminate the synthetic volume producing a near Gaussian light intensity distribution on the spherical particles. This approach is similar to the ideal Gaussian light distribution used by Elsinga et al. (2006). In this procedure, the laser sheet is modelled with a uniform distribution in the synthetic volume. This provides a top hat light intensity distribution which is commonly seen in Tomo-PIV experiments by elimination of low-energy fringes on the sides (Scarano and Poelma 2009). The lighting model is then refined to account for light scattering around the seeding particles. This is necessary as the seeding particles typically used in PIV experiments are in the order of one micrometer in diameter. Therefore, the scattering of light from these particles fall in the Mie regime (Tropea et al. 2007). This phenomenon occurs when the particle diameter ($d_p$) is comparable to the wavelength of light ($\lambda$) in the laser sheet ($d_p \approx \lambda$) (Bohren and Huffman 1983). To account for this effect, we modelled the angular scattering function as shown in Fig. 3. This defines the intensity of light scattered by a spherical object depending on the position of the observer (camera). An algorithm developed by Matzle (2002) is implemented to determine this function based on $d_p$, $\lambda$ and the refractive index of the particles for each simulation.

In our simulations, the angular scattering function is generated using typical PIV experimental parameters where particle diameter is 1–4 μm and the wavelength of green laser light is 532 nm. The flow medium is modelled as air, and the seeding particles are considered to be oil based for the Mie-scatter model. A polynomial function is then curve-fitted to determine a smooth scaling factor, which is then used to scale the intensity of light that can be detected from various camera positions. Once the required parameters of each camera and lighting are set correctly in the simulation, synthetic images of the volume are captured. Figure 4 is a typical image of a synthetic volume imaged at a particular camera position and orientation. To simulate the effect of camera noise, a white Gaussian noise signal corresponding to 10% of the global peak particle intensity across all the cameras is used (Worth et al. 2010; Elsinga et al. 2006). It should be noted that the noise is added prior to application of the Mie scatter model in each synthetic image, as the camera noise is independent of the scattering angle. Therefore, the signal-to-noise ratio in each camera varies based on orientation and position.

### 2.3 Reconstruction

The synthetic images are pre-processed prior to reconstruction using a histogram-based thresholding technique. This technique attempts to determine the range of image intensities that is dominant for a given image, and filter the rest of the outlying intensities. It is noted that a normalisation technique is not used throughout this paper on the synthetic images. Such a normalisation was tested and found to have minimal effect on the reconstruction quality. This is primarily because here we use a uniform light intensity distribution across the synthetic volume. In addition, normalisation would scale the intensity of both the particles and noise present in an image. Thus, the signal-to-noise ratio of an image will remain constant.

The reconstruction procedure utilises a multiplicative line-of-sight technique, where each voxel position within the synthetic volume is mapped onto pixel coordinates on the synthetic images. This result is then further refined for improved accuracy. The MLOS-SMART algorithm has been shown by Atkinson and Soria (2009) to have equivalent reconstruction quality to MART (Elsinga et al. 2006). To perform the reconstruction, physical space coordinates

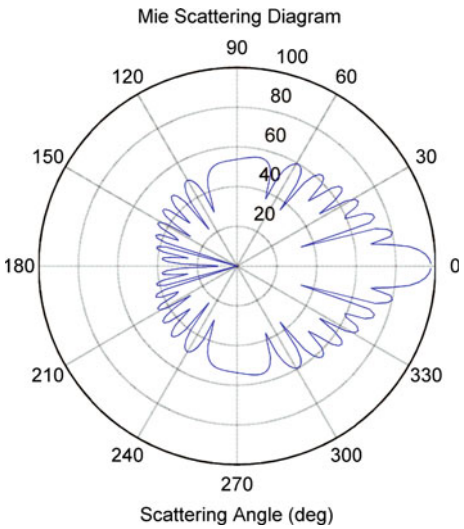


**Fig. 3** A typical 'Mie scatter' angular function

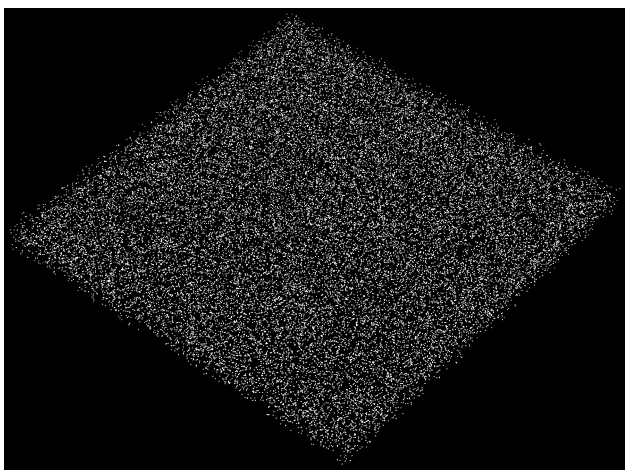

**Fig. 4** Image of the synthetic particles within the simulation volume

of the synthetic volume is mapped to the corresponding pixel position locations in each camera using the calibration coefficients. Thereafter, an interpolation scheme is used to obtain the intensity of each voxel. The use of an interpolation scheme was suggested by Atkinson and Soria (2009), however, previously a nearest neighbor interpolation scheme was used to determine the intensity level to an order of one pixel. In our study, we use a bi-cubic interpolation scheme to determine the intensity of each voxel to sub-pixel accuracy in the image. This procedure is computationally intensive; therefore, the interpolation is parallelised to reduce processing time.

Once the intensity level at each voxel is determined, an intensity matrix ($I_{t_1}$) within the region of the synthetic volume is obtained for a given set of particle positions. The synthetic particles are then displaced individually based on the DNS velocity field data prior to capturing a second set of images, which corresponds to the second exposure in a double frame PIV camera. Therefore, the displacement of each particle is determined to first-order accuracy. It is noted here that the simulation results are obtained over only one realisation of the DNS data and therefore are not converged as compared to long-time averaged results. However, here we are purely interested in a comparison to a given DNS result. Since the particles are randomly distributed within the synthetic volume, a tri-linear interpolation is performed on the DNS data to determine the displacement of each particle at its given position. This additional interpolation introduces an error generally not present in a Tomo-PIV experiment. However, because of the high spatial resolution of the DNS data, the discrepancy due to this interpolation is several orders of magnitude smaller than the overall inaccuracy associated with the Tomo-PIV technique. Once the particle displacements are known, the reconstruction procedure is repeated to determine a second intensity matrix ($I_{t_2}$) for the synthetic volume at $t_2 = t_1 + \delta t$, where $\delta t$ corresponds to the time lag between the two sets of images.

### 2.4 Three-dimensional cross-correlation

The cross-correlation is primarily based on a 'template matching' scheme based on Lewis (1995) and in addition incorporates several advancements discussed in Scarano (2001) to the cross-correlation techniques of PIV images. The normalised correlation coefficient (NCC) equation stated in Lewis (1995) is expanded to perform a three-dimensional template matching between the two reconstructed intensity matrices in the frequency domain as documented by Willert and Gharib (1991). The NCC ($\gamma$) is calculated using

$$\gamma(x_T, y_T, z_T) = \frac{\sum_{x,y,z}\left\{[F(x,y,z) - \overline{F}_{x_T,y_T,z_T}][T(x-x_T, y-y_T, z-z_T) - \overline{T}]\right\}}{\left\{\sum_{x,y,z}[F(x,y,z) - \overline{F}_{x_T,y_T,z_T}]^2 \sum_{x,y,z}[T(x-x_T, y-y_T, z-z_T) - \overline{T}]^2\right\}^{0.5}} \quad (3)$$

to voxel accuracy, where $F$ is the image (intensity matrix at the second exposure) and the sum is over $x$, $y$, $z$ under the interrogation volume containing the feature $T$ (interrogation volume from the intensity matrix at the first exposure) positioned at $x_T, y_T, z_T$. $\overline{T}$ is the mean of the feature and $\overline{F}_{x_T,y_T,z_T}$ is the mean of $F(x, y, z)$ in the region under the feature (Lewis 1995).

A multi-step/sub-pixel technique is then used to determine the location of the normalised cross-correlation peak to sub-pixel accuracy as discussed in Scarano (2001). This information then provides the displacement of each interrogation volume in three-dimensional space within the synthetic volume. To ensure that the global maximum of the NCC is present in the search volume for each interrogation volume, a multi-pass approach is adopted where the search volume is increased iteratively, thereby avoiding any loss of pairs. Furthermore, this technique ensures that for a given interrogation volume, the minimal search region is used reducing overall processing time. This technique is discussed in further detail by Adrian (1991); Fincham and Spedding (1997); Westerweel (1997, 2000); Gui and Merzkirch (2000) and Gui et al. (2001).

## 3 Results

Each simulation provides the three velocity components $U$, $V$, $W$ within the synthetic volume. The velocity field consists of 200 × 200 × 12 velocity vectors corresponding to approximately $5 \times 10^5$ velocity vectors within the synthetic volume. From this information, we are able to determine statistics of the flow such as the mean ($\overline{U}^+$) and the standard deviations ($u'^+, v'^+$ and $w'^+$). The same parameters are then determined from the DNS data, this is done by determining $U$, $V$, $W$ at the same interrogation volume positions which ensures that a relative comparison is made between the tomographic-PIV technique and DNS.

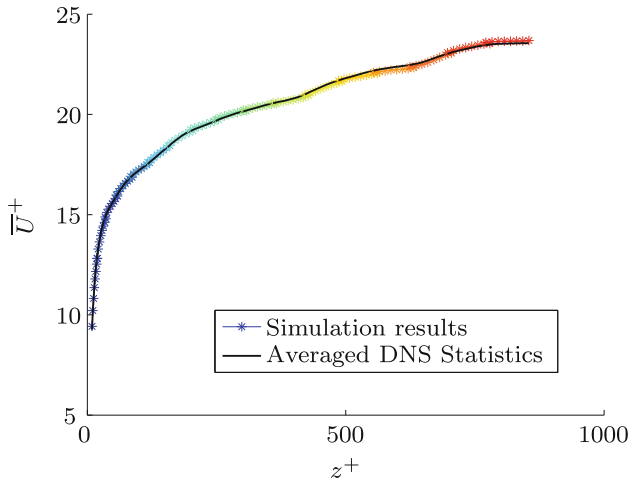


**(a)** $l_v^+ = 0.94$

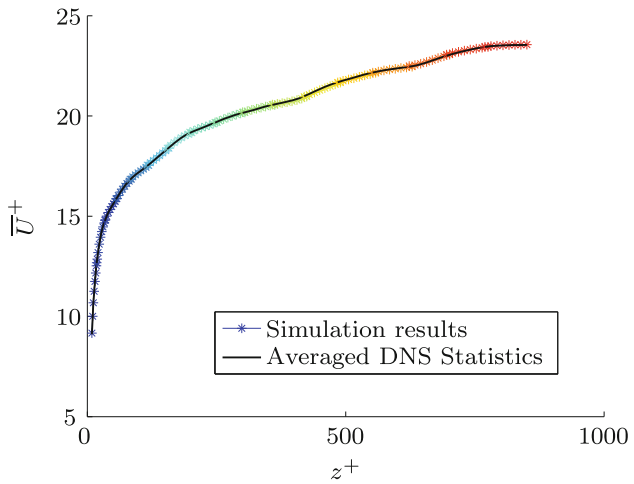


**(b)** $l_v^+ = 0.63$

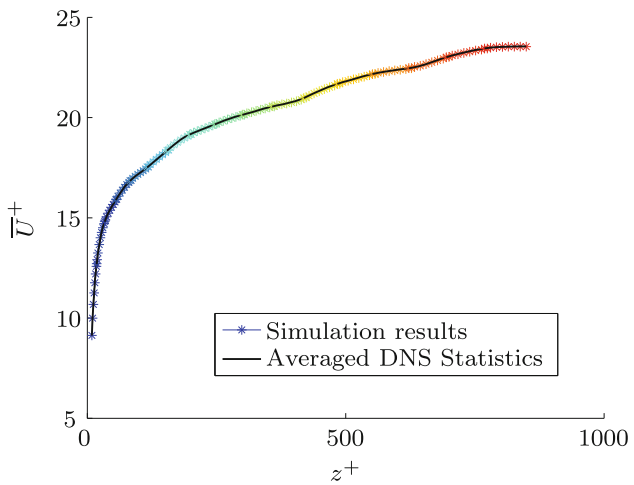


**(c)** $l_v^+ = 0.47$

**Fig. 5** Comparison of simulation results (*colours* indicate a single simulation with a $\delta z^+ \approx 100$) and DNS statistics for the mean velocity ($\overline{U}^+$) at **a** $l_v^+ = 0.94$, **b** $l_v^+ = 0.63$ and **c** $l_v^+ = 0.47$

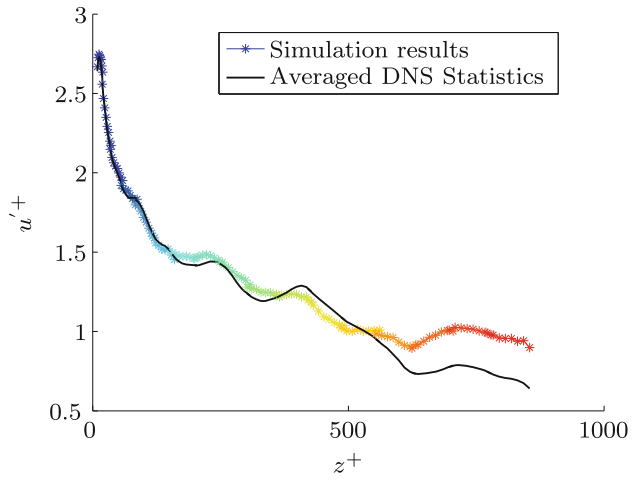


**(a)** $l_v^+ = 0.94$

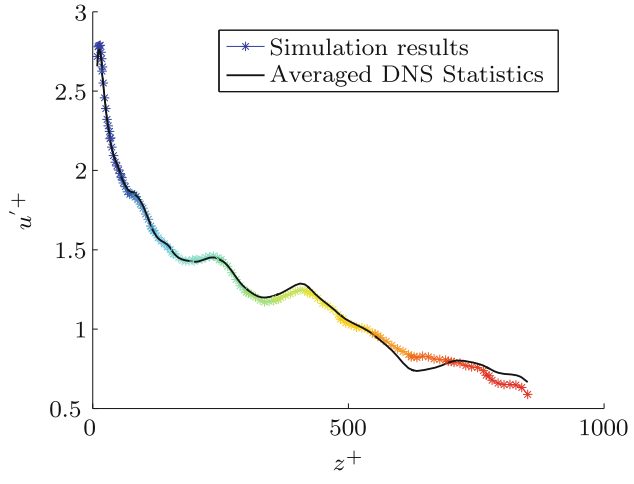


**(b)** $l_v^+ = 0.63$

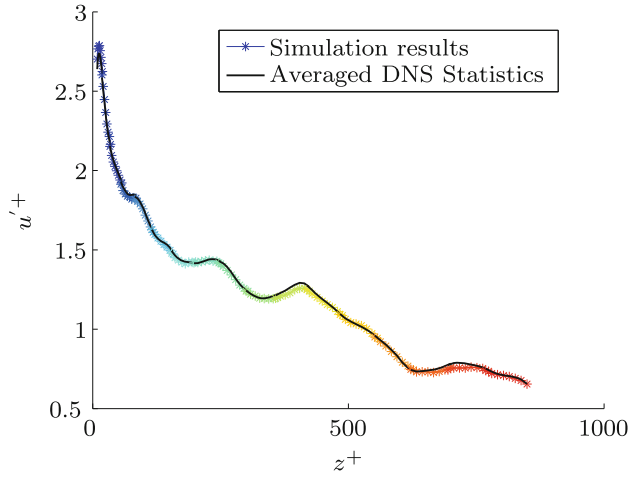


**(c)** $l_v^+ = 0.47$

**Fig. 6** Comparison of simulation results (*colours* indicate a single simulation with a $\delta z^+ \approx 100$) and DNS statistics for the rms of streamwise velocity ($u'^+$) at **a** $l_v^+ = 0.94$, **b** $l_v^+ = 0.63$ and **c** $l_v^+ = 0.47$

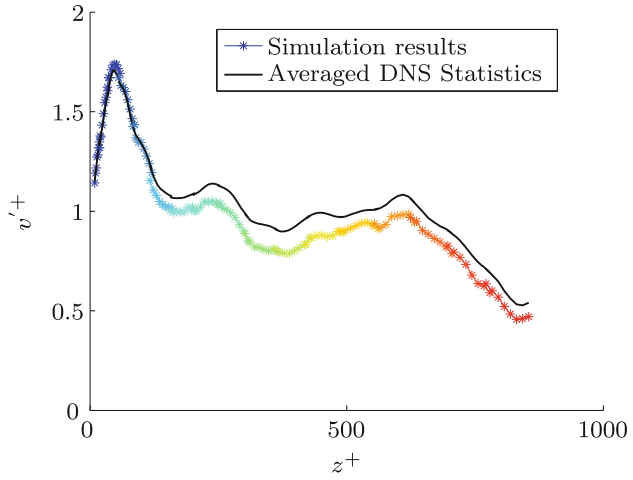


**(a)** $l_v^+ = 0.94$

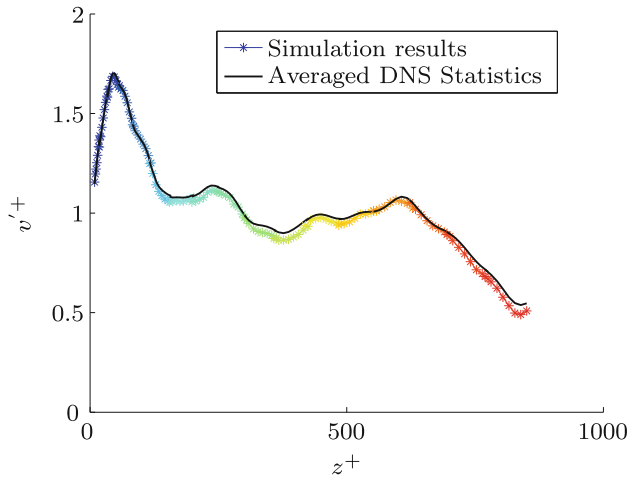


**(b)** $l_v^+ = 0.63$

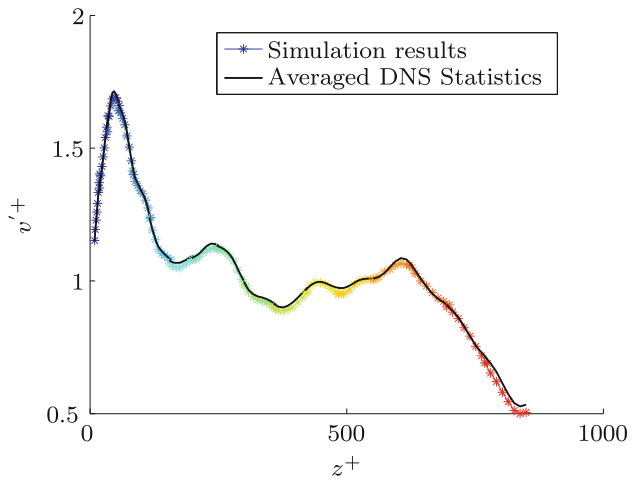


**(c)** $l_v^+ = 0.47$

**Fig. 7** Comparison of simulation results (*colours* indicate a single simulation with a $\delta z^+ \approx 100$) and DNS statistics for the rms of spanwise velocity ($v'^+$) at **a** $l_v^+ = 0.94$, **b** $l_v^+ = 0.63$ and **c** $l_v^+ = 0.47$

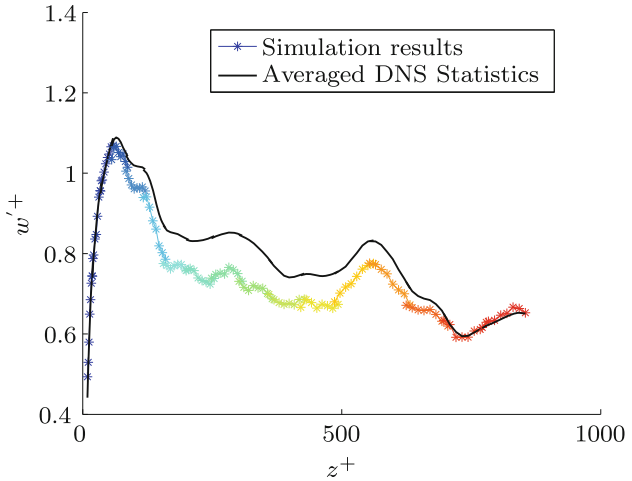


**(a)** $l_v^+ = 0.94$

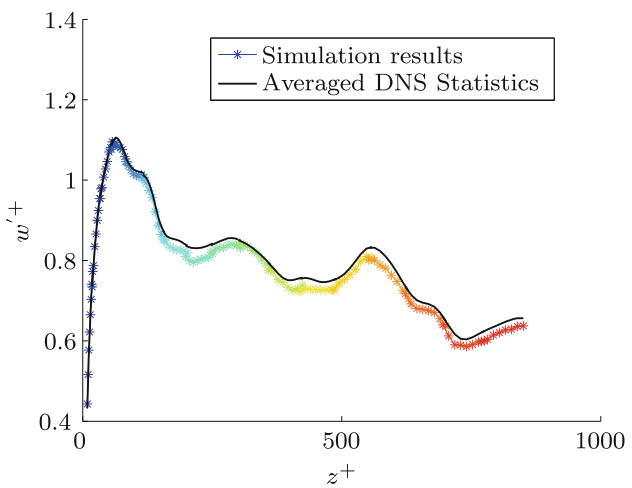


**(b)** $l_v^+ = 0.63$

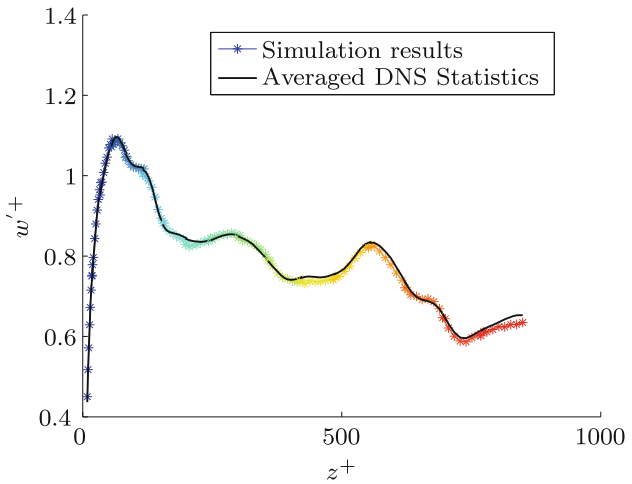


**(c)** $l_v^+ = 0.47$

**Fig. 8** Comparison of simulation results (*colours* indicate a single simulation with a $\delta z^+ \approx 100$) and DNS statistics for the rms of wall-normal velocity ($w'^+$) at **a** $l_v^+ = 0.94$, **b** $l_v^+ = 0.63$ and **c** $l_v^+ = 0.47$

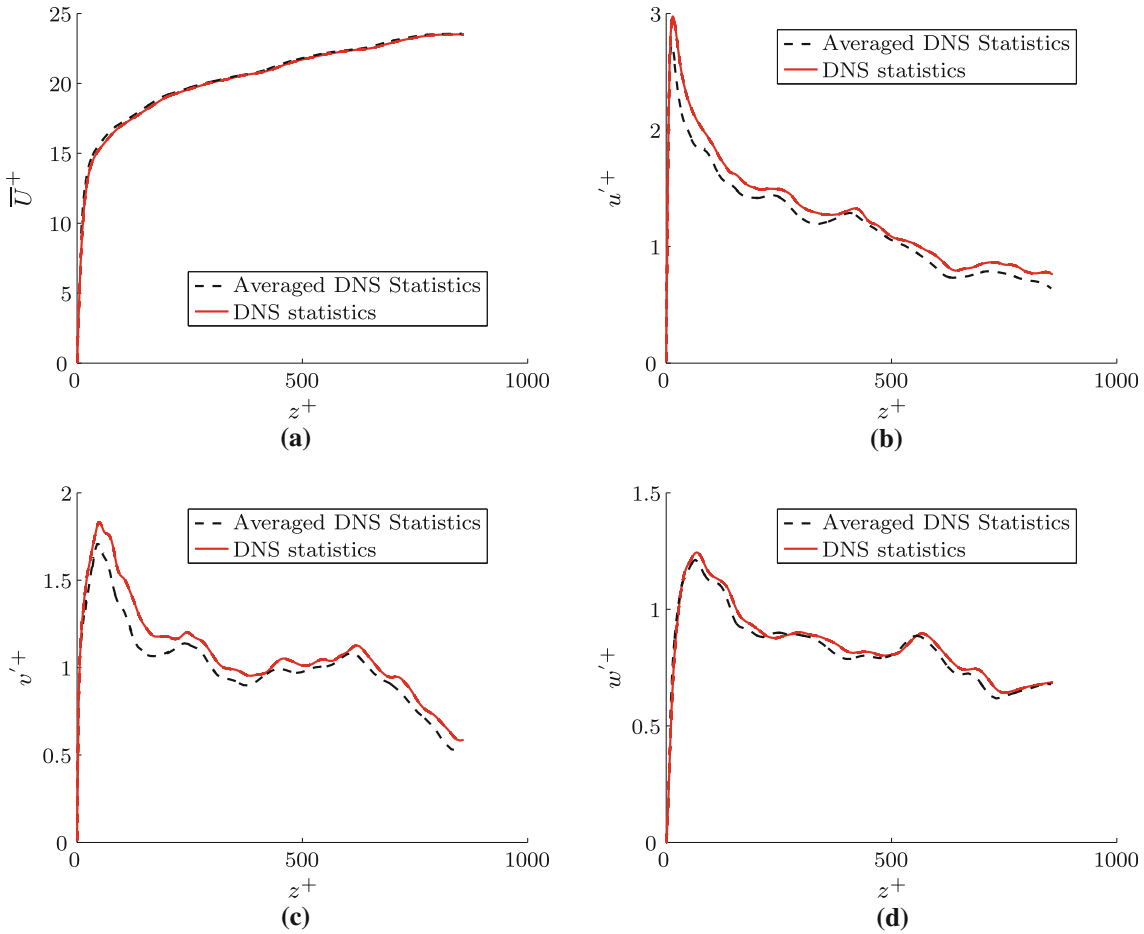


**Fig. 9** Comparison of averaged DNS statistics and DNS statistics (del Alamo et al. 2004) for **a** $\overline{U}^+$, **b** $u'^+$, **c** $v'^+$ and **d** $w'^+$. The averaged DNS results are over an interrogation volume length of $l^+ = 20$ to mimic the Tomo-PIV experiments

**Table 1** Summary of percentage errors for flow statistics in the region $100 < z^+ < 200$ with an interrogation volume length of $l^+ = 20$

| Voxel size ($l_v^+$) | 0.94 | 0.63 | 0.47 |
|---|---|---|---|
| Tomo-PIV simulation vs. averaged DNS statistics | % | % | % |
| $\overline{U}^+$ | 0.43 | 0.17 | 0.08 |
| $u'^+$ | 3.99 | 1.47 | 0.44 |
| $v'^+$ | 7.42 | 1.55 | 1.05 |
| $w'^+$ | 7.53 | 2.41 | 1.10 |
| Tomo-PIV simulation vs. DNS statistics | % | % | % |
| $\overline{U}^+$ | 0.95 | 0.65 | 0.09 |
| $u'^+$ | 4.68 | 3.62 | 2.06 |
| $v'^+$ | 11.22 | 5.59 | 5.06 |
| $w'^+$ | 12.69 | 7.57 | 6.40 |

### 3.1 Volume discretisation (Voxel size)

The simulations are run at several volume discretisation levels while all other parameters are kept constant. For example, an interrogation volume length of $l^+ = 20$ and $N_I \approx 5$ is used in each case to ensure the seeding particle movement is approximately 25% of the interrogation volume length with constant seeding density. This satisfies the quarter voxel displacement criterion suggested by Keane and Adrian (1992). In addition, the voxel to pixel size ratio in all simulations is approximately equal to one as suggested by Elsinga et al. (2006). The DNS data is applied to the synthetic volume in steps of $\delta z^+ \approx 100$ corresponding to the laser sheet thickness. A symmetric four camera configuration is used, positioned with an azimuthal angle $\theta = 25°$ and an elevation angle $\phi = 55°$. To visualise the accuracy at varying volume discretisation levels, flow statistics $\overline{U}^+, u'^+, v'^+$ and $w'^+$ are presented in Figs. 5, 6, 7

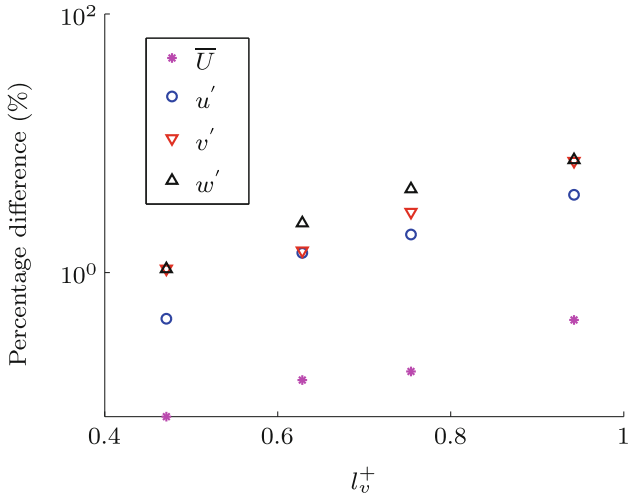


**Fig. 10** Accuracy for varying voxel sizes for statistics in the region $100 < z^+ < 200$ with an interrogation volume length of $l^+ = 20$, compared to averaged DNS statistics

and 8, respectively. Each sub figure consists of simulation results and DNS statistics averaged over the same interrogation volume positions of each simulation (averaged DNS statistics). Figure 9 shows a comparison between averaged DNS statistics and DNS statistics (del Alamo et al. 2004) for $\overline{U}^+, u'^+, v'^+$ and $w'^+$ evaluated at the center of each interrogation volume. A clear attenuation between these statistics is seen in $u'^+, v'^+$ and $w'^+$ in Fig. 9b–d, respectively, since the DNS data is spatially averaged over the interrogation volume. This is consistent with the spatial attenuation in the streamwise fluctuating velocity component $u$ observed in hot-wire anemometry measurements by Hutchins et al. (2009). However, no attenuation between the 'averaged DNS statistics' and the simulation results is present in Figs. 6, 7 and 8 since the spatial averaging is equivalent. Furthermore, the 'averaged DNS statistics' provide an upper limit on the accuracy that can be achieved for the current simulation parameters. As expected it can be seen that with increasing spatial resolution the accuracy increases. This is particularly evident in the second-order statistics.

Table 1 gives a summary of comparisons between simulation results and the DNS statistics in the log region $100 < z^+ < 200$. It can be seen that the mid-range discretisation level of $l_v^+ = 0.63$ is sufficient to obtain an error less than 3% in the second order statistics $u'^+, v'^+$ and $w'^+$ in comparison to the averaged DNS statistics. Increasing the discretisation level to $l_v^+ = 0.47$ we can obtain an average error less than 1.5%. Attenuation of hot-wire anemometry statistics using spanwise spatial averaging of the same DNS data used in this study was performed by Chin et al. (2010). Results obtained in these two simulation studies suggest that the attenuation at the location of the peak turbulence intensity ($z^+ \approx 15$) for $u'^+$ is approximately twice for Tomo-PIV in comparison with hot-wire anemometry. This comparison is made with a spanwise spatial averaging length of approximately 20 viscous inner length units in both simulations. Furthermore, from Table 1, it can be seen that at all volume discretisation levels the accuracy in $v'^+$ and $w'^+$ is lower than $u'^+$. This difference in accuracy between the velocity components is due to the lower voxel displacement in the wall-normal and spanwise direction in comparison with the streamwise direction. This leads to a reduced accuracy in the sub-pixel estimation in the cross-correlation phase. In addition, the wall-normal velocity component is determined along the thickness of the laser sheet ($z$). This direction is most hindered by limitations of tomographic PIV, such as Gaussian shaped laser sheet intensity and poor reconstruction quality in depth due to typical camera configurations used. To minimise the effect of these limitations, it is essential that camera orientation and position is optimised for all Tomo-PIV experiments to obtain the best possible reconstruction quality. This is further discussed in Sect. 3.3.

In Figs. 6a, 7a and 8a a larger magnitude of error is noticeable in the second-order statistics at lower spatial resolutions away from the wall ($z^+ > 500$). This can be attributed to two factors. Firstly, further away from the wall although the mean velocity is higher, the fluctuations in the velocity components are smaller and generally less than movements of the order $l_v^+$. This leads to an inaccurate peak detection in the cross-correlation procedure. Secondly, the time between the two snapshots ($\delta t$) was optimised in the region $100 < z^+ < 200$ for this analysis. This parameter is then kept constant for all other simulations; therefore, we would expect more erroneous data away from this region. Figure 10 shows the gain in accuracy with increasing spatial resolution or reducing $l_v^+$ in comparison with the

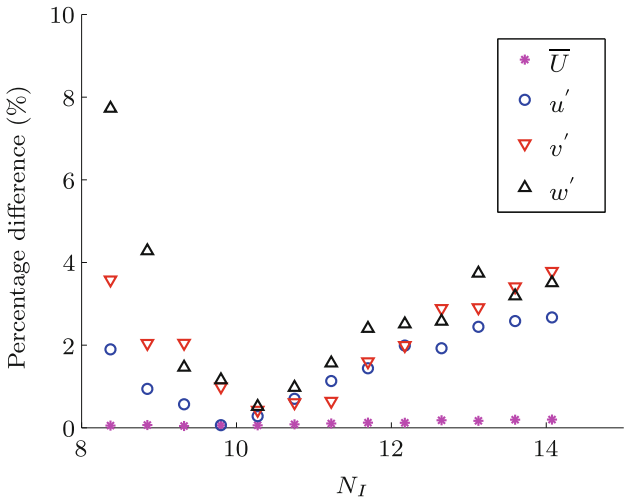


**Fig. 11** Comparison between simulation results and averaged DNS statistics at varying particles per interrogation volume ($N_I$) for an interrogation volume length of $l^+ = 20$

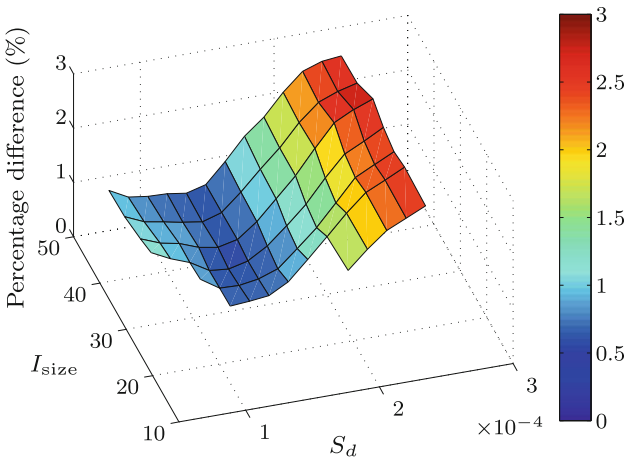


**Fig. 12** Comparison between simulation results and averaged DNS statistics for $u'^{+}$ for varying seeding density ($S_d$) and interrogation volume size ($I_{size} = I_x, I_y, I_z$)

averaged DNS statistics. From these results it can be seen that on a logarithmic scale the increase in accuracy is approximately linear with $l_v^+$. Therefore, it is recommended that a value of $l_v^+ \approx 0.6$ is sufficient to obtain an acceptable accuracy of within 3% for first- and second-order flow statistics in comparison with the averaged DNS statistics. This corresponds to a particle diameter of approximately three pixels, which also satisfies the optimal particle size in pixels for PIV experiments given by Adrian (1991). Although increasing the spatial resolution further would improve the reconstruction quality, the improvement does not outweigh the disadvantages previously stated. Furthermore, to obtain the volume discretisation levels considered in this simulation study, the pixel size on the sensor should be selected within the typical range used for PIV experiments (7–12 μm Overmars et al. 2010) to ensure adequate light sensitivity (Chen et al. 2000).

### 3.2 Particles per interrogation volume ($N_I$) and seeding density

To investigate the influence of the particles per interrogation volume and seeding density, simulations are run with varying number of synthetic particles and interrogation volume size while keeping all other parameters constant. The simulations are performed with a symmetric four camera setup positioned with an azimuthal angle $\theta = 25°$ and an elevation angle $\phi = 55°$. In addition, a constant volume discretisation level of $l_v^+ \approx 0.6$ is used, and the DNS data applied to the synthetic volume is in the region $100 < z^+ < 200$. Figure 11 shows the percentage difference of the flow statistics between the simulation and DNS results for varying $N_I$. These results suggest there is a region where the accuracy is optimal. This occurs at $N_I \approx 10$ for the current interrogation volume length of $l^+ = 20$. A similar analysis was conducted by Adrian (1991) and Elsinga et al. (2006) for 2D-PIV with a comparable result. Furthermore, we can conclude that when $N_I > 15$ there is a substantial reduction in accuracy due to saturation of the camera images caused by off-plane particle overlap (Belden et al. 2010). As expected, the results show that the accuracy for the mean statistics is significantly higher than for the second-order statistics. It can also be seen that the inaccuracy of $w'^{+}$ is higher than the equivalent stream-wise component $u'^{+}$, which is consistent with results presented in Sect. 3.1. However, if one considers other interrogation volume sizes, the optimal $N_I$ is found not to be universal. Instead a ratio between $N_I$ and the interrogation volume size, $S_d$, is calculated using

$$S_d = \frac{N_I}{I_x I_y I_z}, \tag{4}$$

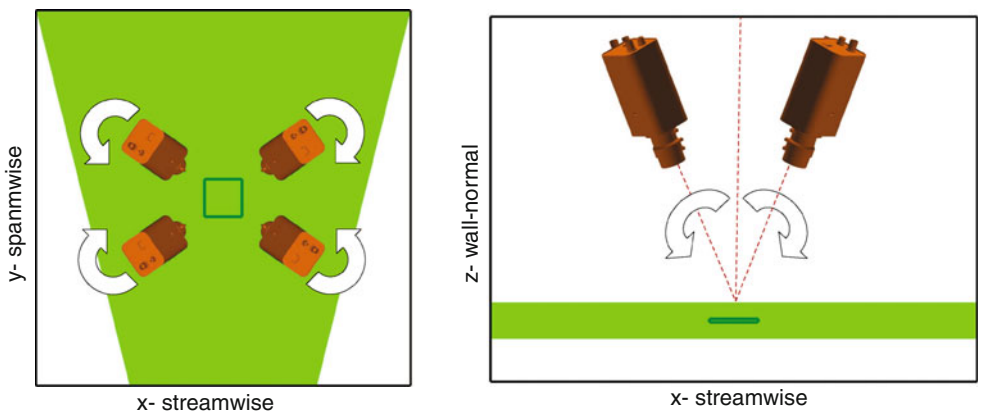


**(a)** Variation of azimuthal angle

**(b)** Variation of elevation angle

**Fig. 13** Variation of camera position

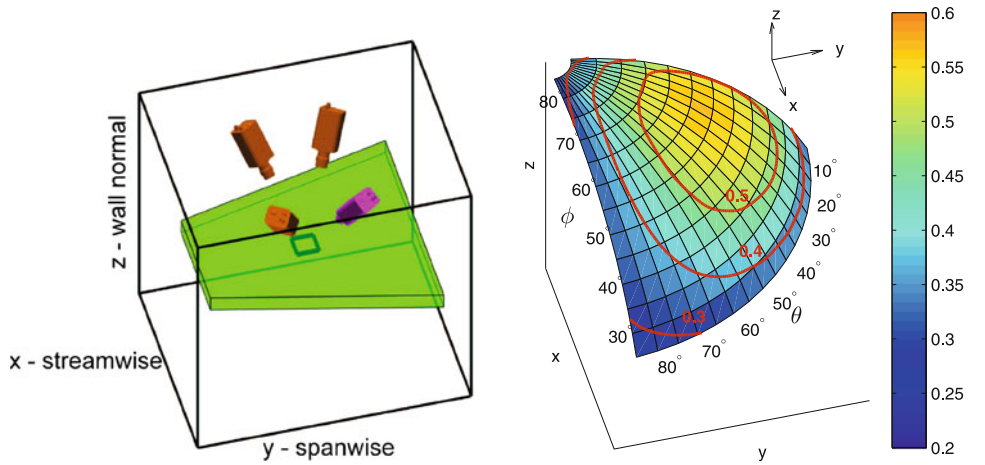


**(a)** Camera configuration

**(b)** Plot of reconstruction quality $Q$ for the camera indicated by magenta

**Fig. 14** All cameras placed on a single side of laser Top view/Bottom view camera configuration

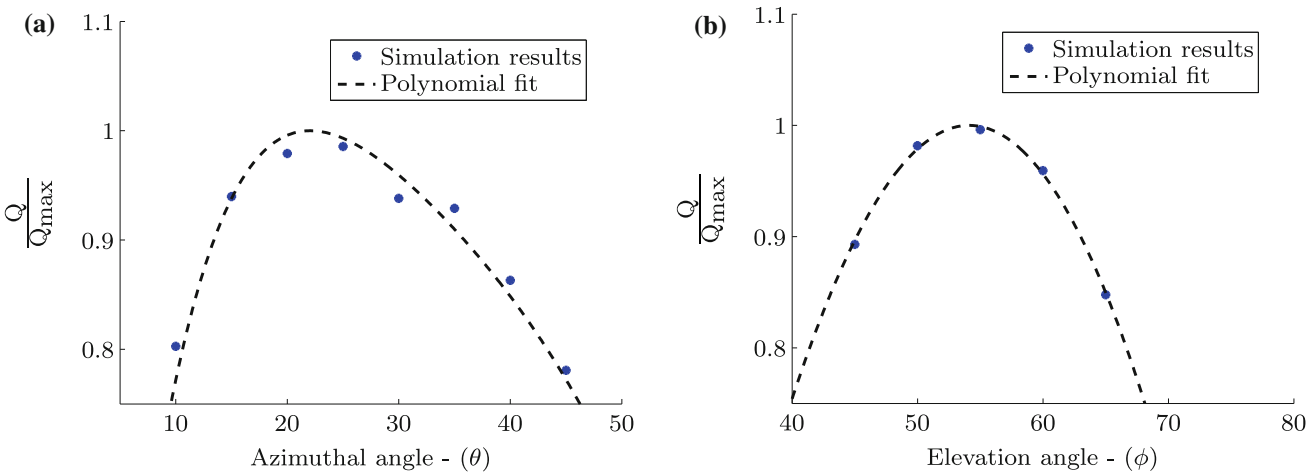


**Fig. 15** Plot of reconstruction quality $Q/Q_{max}$ at **a** the optimal elevation ($\phi = 55°$) for varying azimuthal angles ($\theta$) and **b** the optimal azimuthal angle ($\theta = 25°$) at varying elevation angles ($\phi$)

where $I_x$, $I_y$, $I_z$ are the interrogation volume sizes in voxels in the $x$, $y$, $z$ directions, respectively. Figure 12 presents results obtained for the accuracy in $u'^+$ between simulation and averaged DNS statistics for varying interrogation volume sizes and seeding density $S_d$. It is evident that $S_d \approx 1.4 \times 10^{-4}$ provides the optimal accuracy that remains consistent for varying interrogation volume sizes. Therefore, we propose that this value of $S_d$ can be used as a reference to determine the required seeding density at a certain interrogation volume size. It should be noted that simulation results were omitted at low seeding densities which lead to highly erroneous results due to insufficient seeding particles for an accurate cross-correlation. Similarly, low interrogation volume sizes of the order of the average streamwise voxel displacement lead to inaccurate peak detections (Keane and Adrian 1992).

### 3.3 Camera position and orientation

To simulate the effect of moving each camera in three-dimensional space, we consider adjusting each camera's azimuthal and elevation angles as shown in Fig. 1. The simulations are run for a four-camera setup that is positioned as shown in Fig. 13 to maintain symmetry in the four quadrants. Each camera is placed using a spherical coordinate system where the radial distance is kept constant and the angles $\theta$ and $\phi$ are varied. A constant volume discretisation level of $l_v^+ \approx 0.6$ is used and all other simulations parameters are consistent with Sect. 3.1. To

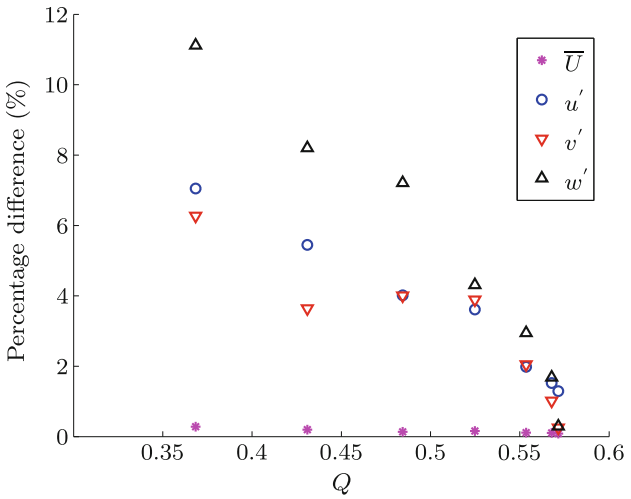


**Fig. 16** Comparison between simulation results and averaged DNS statistics at varying reconstruction quality ($Q$) (for $\phi = 55°$ with varying $\theta$) for an interrogation volume length of $l^+ = 20$

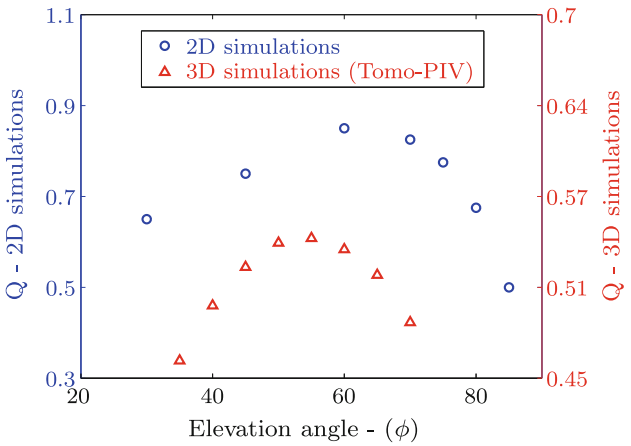


**Fig. 17** Comparison between 2D simulations results obtained by Elsinga et al. (2006) and the Tomo-PIV simulation results at $\theta = 25°$

perform a quantitative analysis on how well the intensity field is reconstructed in each simulation, the reconstruction quality $Q$ is determined using

$$Q = \frac{\sum_{x,y,z} E_1(x,y,z).E_0(x,y,z)}{\sqrt{\sum_{x,y,z} E_1^2(x,y,z).\sum_{x,y,z} E_0^2(x,y,z)}} \quad (5)$$

where $E_1(x, y, z)$ is the reconstructed intensity matrix, and $E_0(x, y, z)$ is an ideal reconstruction intensity matrix based on known particle positions (Elsinga et al. 2006).

### 3.3.1 *Top view/bottom view camera configuration*

This configuration consists of all cameras placed on one side of the laser sheet as shown in Fig. 14, which is the most common configuration used as it is typically easiest to setup. The camera lens is placed at a constant radial distance of $5000^+$ (5000 inner viscous length units) away from the synthetic target with a light sheet thickness of $100^+$, centered at the origin ($x, y, z = 0$). The azimuthal angle and elevation angle are varied from 5°–85° and 20°–85°, respectively, to determine the reconstruction quality $Q$ at each position. Elevation angles below 20° are not considered as this places the cameras at a highly skewed angle in relation to the illuminated volume, causing the synthetic volume to be encapsulated in a small region within the field of view in each camera. In addition, a typical Scheimpflug adapter will not be able to align the focal plane of the camera and the mid-plane of the synthetic volume in such cases. Figure 14 shows the variation of $Q$ at each camera position and orientation. The results are only presented from one quadrant, since the four cameras are placed and moved while maintaining symmetry.

Figure 15 shows the variation in $Q$, normalised by the maximum obtainable $Q$ ($Q_{max}$) for the given configuration. This is obtained by fitting a polynomial to a slice of the simulation results at the optimal azimuthal ($\theta \approx 23°$) and elevation ($\phi \approx 55°$) angles. Figure 15 shows that within the range of $50° < \phi < 60°$ and $20° < \theta < 25°$, a $Q$ greater than 95% of $Q_{max}$ is obtained. It should be noted that within this range of angles, the ratio between the camera noise and the peak particle intensity of each camera is approximately 11% and 16% for cameras placed in forward and backward scatter postions, respectively. A further deviation from this range by ±5° reduces $Q$ to 90% of $Q_{max}$. Thereafter, the decline in $Q$ increases rapidly; therefore, it is recommended to not exceed this range.

Figure 16 shows the variation in accuracy of flow statistics at varying reconstruction quality $Q$ for $\phi = 55°$ with varying $\theta$. This comparison enables us to quantify the variation in accuracy of flow statistics due to $Q$. These results suggest a clear improvement in the accuracy of the flow statistics as $Q$ increases. Results obtained for the optimal range for the elevation angle can be compared against previous studies by Elsinga et al. (2006) from simulations run on a two dimensional synthetic volume. Figure 17 gives a comparison of $Q$ between 2D simulation results obtained by Elsinga et al. (2006) and a slice of the simulation results obtained in this study at $\theta = 25°$. Results are presented on different vertical axis scales in this comparison to enhance the similarity in the trend of $Q$ at different elevation angles. In addition, it should be noted that values obtained for $Q$ are lower than that observed by Elsinga et al. (2006) using 2D simulations which gives a maximum possible value of $Q \approx 0.85$ at $\phi \approx 60°$, while the 3D simulations have a maximum value of $Q \approx 0.55$ at $\phi \approx 55°$. This is expected as the simulations in this analysis models a 3D reconstruction which results in a fundamental reduction in reconstruction quality $Q$ as

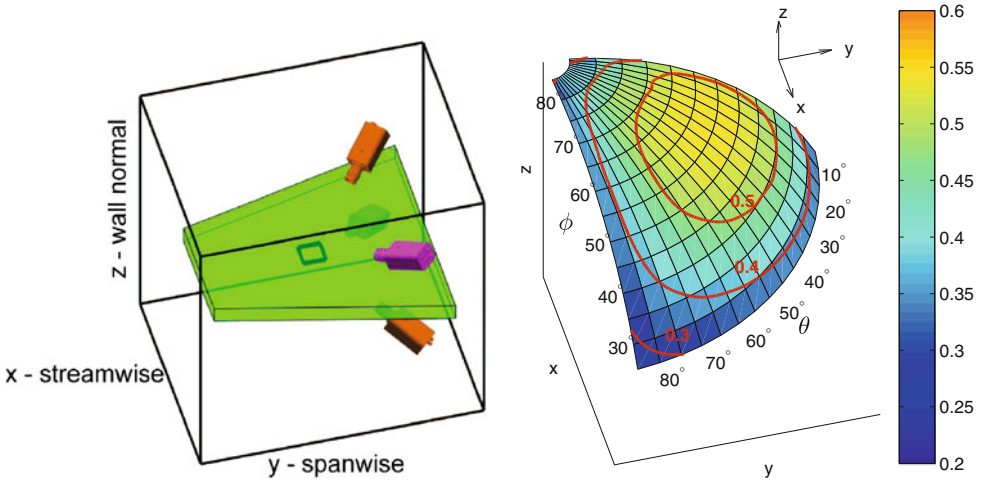


**(a)** Camera configuration

**(b)** Plot of reconstruction quality $Q$ for the camera indicated by magenta

**Fig. 18** All cameras placed facing towards illumination source (Forward scatter configuration)

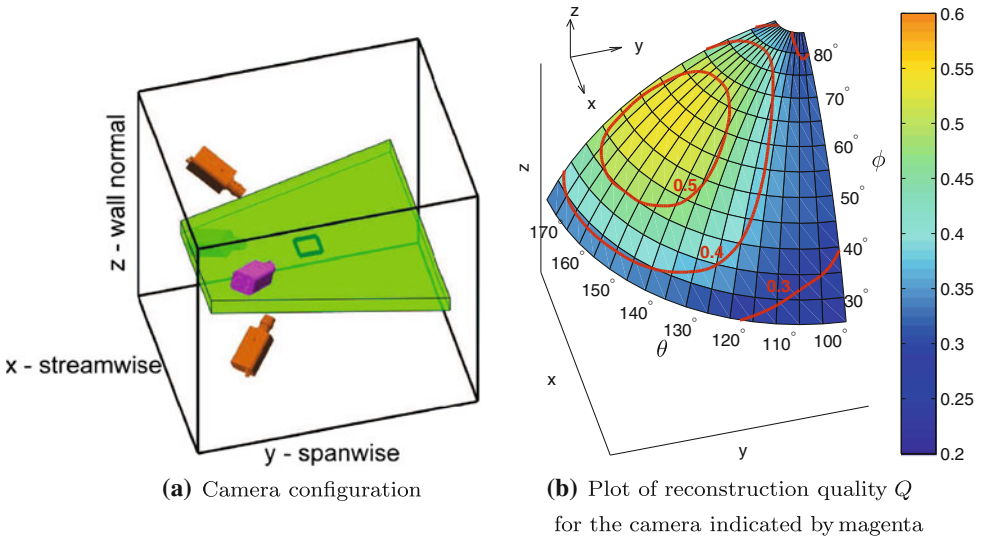


**(a)** Camera configuration

**(b)** Plot of reconstruction quality $Q$ for the camera indicated by magenta

**Fig. 19** All cameras placed facing away from illumination source (Backward scatter configuration)

demonstrated by Elsinga et al. (2006). In addition, the simulations include a calibration procedure, image distortion, Mie scattering and camera noise, all of which contribute to a further reduction in $Q$. However, our simulation provides an improved representation of the actual quality observed in a typical tomographic experiment.

It is also evident that when considering the azimuthal angle, optimal results are obtained between 20° and 25°. Therefore, the reconstruction quality is not symmetric about $\theta = 45°$. This is caused by the scaling of each synthetic image based on a 'Mie scattering' model which increases the mean intensity of synthetic images captured from a camera at $\theta < 45°$ where the camera is positioned at a forward scatter position relative to the illumination model. This phenomenon is evident in the results presented in Figs. 13 and 15 as we see improved results in the range where $\theta < 45°$ compared to $\theta > 45°$. Furthermore, it should be noted that the optimum camera position maybe affected if the flow medium or the type of seeding particle is varied.

### *3.3.2 Forward and backward scatter configuration*

These two configurations include simulations where all four cameras are placed in a forward and backward scatter configuration in relation to the direction of the laser, as shown in Figs. 18 and 19, respectively. Spherical objects used to emulate the seeding particles scatter more light in

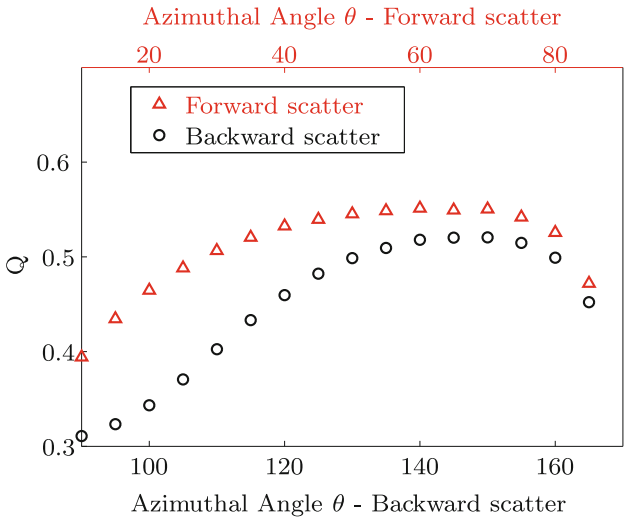


**Fig. 20** Comparison of reconstruction quality between forward and backward scatter at $\phi = 55°$ for varying azimuthal angles ($\theta$)

the forward scatter direction (Bohren and Huffman 1983). This is evident by comparing the contours on Figs. 18 and 19. Furthermore, by comparison at a single elevation angle of $\phi = 55°$ as shown in Fig. 20 the forward scatter configuration consistently gives a better reconstruction (higher $Q$) by approximately 10%. A sharp decrease in quality is noted for $\theta < 45°$ for the backscatter configuration as the mean intensity captured by each camera drops significantly according to the 'Mie scatter' model as seen in Table 2. A clear reduction in signal to noise ratio is observed from a forward to a backward scatter configuration when artificial noise is included to model camera noise. This reduction in signal to noise ratio for the backward scatter configuration leads to a lower reconstruction quality $Q$ due to poor noise filtering in comparison to the forward scatter configuration. Furthermore, from the results in Table 2, we can conclude that the percentage difference between forward and backward scatter configuration reduces as we increase the azimuthal angle. This can be attributed to the shape of the angular scattering function as shown in Fig. 21, which represents the scattering of light at different azimuthal angles. This function accounts for reflection of the laser light to enable positioning of cameras in a backward scatter configuration.

### *3.3.3 Symmetric camera configuration*

This configuration consists of cameras placed symmetrically with respect to the laser sheet and illumination direction as shown in Fig. 22a. Figure 22b shows the reconstruction quality $Q$ at the same $\theta$ and $\phi$ range used to analyse the previous configurations. In comparison to the previous configurations, the optimal camera positions seem to be consistent, however a smaller region is encapsulated

**Table 2** Synthetic image statistics for backward and forward scatter configurations at $\phi = 60°$ (statistics have been normalised using the maximum intensity of an ideal reconstruction)

| | Forward scatter | Backward scatter | % Difference |
|---|---|---|---|
| $\theta$ | 70 | 110 | |
| Mean intensity | 0.23 | 0.09 | 49.06 |
| Maximum intensity | 0.29 | 0.15 | 48.26 |
| $\theta$ | 45 | 135 | |
| Mean intensity | 0.49 | 0.27 | 45.69 |
| Maximum intensity | 0.62 | 0.35 | 44.32 |
| $\theta$ | 25 | 155 | |
| Mean intensity | 0.81 | 0.53 | 34.07 |
| Maximum intensity | 1.00 | 0.68 | 32.04 |

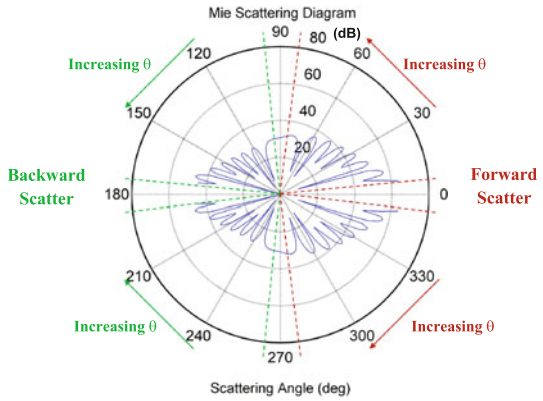


**Fig. 21** Angular scattering function used to model Mie scatter at varying azimuthal angles ($\theta$)

in the $Q = 0.5$ contour line compared to the forward scatter configuration as shown in Fig. 18. This can be attributed to the placement of half the cameras in backward scatter positions. Comparison with the results obtained from the top view/bottom view configuration indicates a minimal variation in the reconstruction quality. Although the symmetric configuration provides an uniform accuracy on both sides of the laser sheet, the top/bottom configuration gives a better reconstruction on the side of the laser sheet on which the cameras are placed. Therefore, the results suggest the benefits from each of these configurations are equal, providing a similar variation in the overall reconstruction quality.

## 4 Conclusions

In this paper, we have analysed several key experimental parameters in a typical tomographic PIV experiment in wall-bounded turbulence. It is shown that several parameters such as the position of each camera, seeding density and

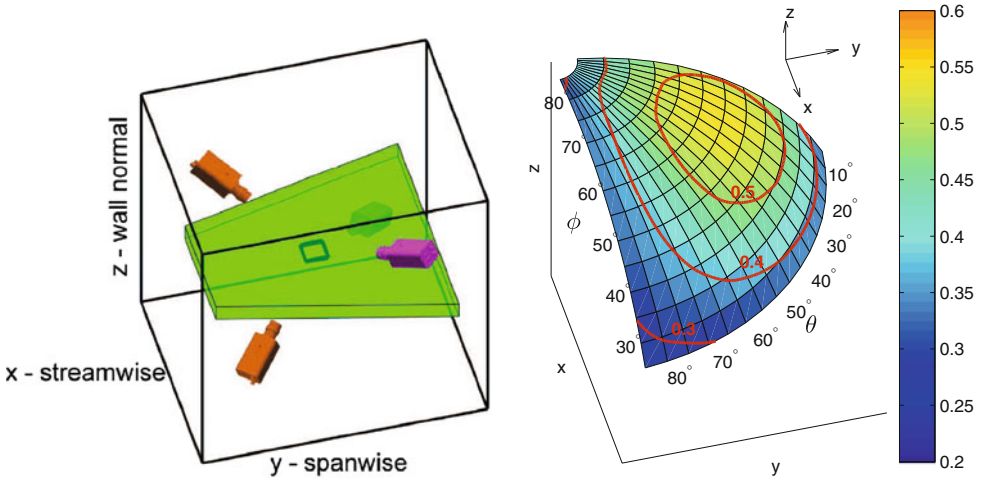


**(a)** Camera configuration

**(b)** Plot of reconstruction quality $Q$ for the camera indicated by magenta

**Fig. 22** All cameras placed symmetrically with respect to the laser sheet and illumination direction (Symmetric configuration)

voxel discretisation level significantly affect the accuracy of tomographic experiments in wall-bounded turbulent flows. We can conclude from the simulations that the optimum camera positions in three-dimensional space for a typical tomographic PIV experiment is $\phi \approx 55°$ measured from the horizontal and $\theta \approx 23°$ measured from the direction of illumination. However, within the range of $50° < \phi < 60°$ and $20° < \theta < 25°$, a $Q$ greater than 95% of $Q_{\max}$ is obtained. Therefore, it is recommended to position each camera within this range. In addition, we recommend the forward scatter and the top view/bottom view configurations based on reconstruction quality. These results were obtained for a four-camera setup with a particular set of camera properties. However, further simulations can be performed for various other camera configurations and properties such as the number of cameras.

The simulations indicate that the parameter $S_d$ which relates to the ratio between particles per interrogation volume and the interrogation volume size has an optimal value of $S_d \approx 1.4 \times 10^{-4}$. This value of $S_d$ can be used as a general guideline for tomographic PIV experiments in wall-bounded turbulent flows to select the required seeding density concentration for a certain interrogation volume size. Furthermore, the simulations showed that depending on the experimental requirements the volume discretisation level can be selected to obtain the necessary accuracy while still minimising expenditure on cameras. In the simulations conducted with an interrogation volume length of $l^+ = 20$ it is seen that a voxel size of $l_v^+ \approx 0.6$ is sufficient to determine the second-order statistics $u'^+, v'^+$ and $w'^+$ with an error less than 2.5% and 7.5% compared with corresponding averaged DNS statistics and DNS statistics (del Alamo et al. 2004) respectively.

The simulations performed in this study can be expanded to assess PIV experiments for various types of flows by applying the appropriate DNS data to the synthetic volume. Additionally, simulations can be performed to assess both two-dimensional and stereoscopic-PIV experimental parameters in a similar methodology as described in this paper to asses these techniques for wall-bounded turbulent flows. The authors wish to gratefully thank Prof. R.D. Moser for making the $Re_\tau = 934$, DNS data available, and the financial support of the Australian Research Council.

## References

Adrian RJ (1991) Particle-imaging techniques for experimental fluid mechanics. Ann Rev Fluid Mech 23:261–304

Arroyo MP, Greated CA (1991) Stereoscopic particle image velocimetry. Meas Sci Technol 2:1181–1186

Atkinson C, Soria J (2009) An efficient simultaneous reconstruction technique for tomographic particle image velocimetry. Exp Fluids 47:553–568

Belden J, Truscott TT, Axiak MC, Techet AH (2010) Three-dimensional synthetic aperture particle image velocimetry. Meas Sci Technol 21(12):125403

Bohren CF, Huffman DR (1983) Absorption and scattering of light by small particles. Wiley, New York

Chen T, Catrysse P, El Gamal A, Wandell B (2000) How small should pixel size be?. Proc SPIE 3965:451–461

Chin C, Hutchins N, Ooi A, Marusic I (2011) Spatial resolution correction for hot-wire anemometry in wall turbulence. Exp Fluids 50:1443–1453

del Alamo JC, Jimenez J, Zandonade P, Moser RD (2004) Scaling of the energy spectra of turbulent channels. J Fluid Mech 500:135–144

Elsinga GE, Scarano F, Wieneke B, van Oudheusden BW (2006) Tomographic particle image velocimetry. Exp Fluids 41:933–947

Fincham AM, Spedding GR (1997) Low cost, high resolution DPIV for measurement of turbulent fluid flow. Exp Fluids 23:449–462
Gui L, Merzkirch W (2000) A comparative study of the MQD method and several correlation-based PIV evaluation algorithms. Exp Fluids 28:36–44
Gui L, Longo J, Stern F (2001) Biases of PIV measurement of turbulent flow and the masked correlation-based interrogation algorithm. Exp Fluids 30:27–35
Hinsch KD (2002) Holographic particle image velocimetry. Meas Sci Technol 13:R61–R72
Hori T, Sakakibara J (2004) High-speed scanning stereoscopic PIV for 3D vorticity measurement in liquids. Meas Sci Technol 15:1067–1078
Hutchins N, Nickels TB, Marusic I, Chong MS (2009) Hot-wire spatial resolution issues in wall-bounded turbulence. J Fluid Mech 635:103–136
Keane RD, Adrian RJ (1992) Theory of cross-correlation of PIV images. Appl Sci Res 49:191–215
Lecordier B, Westerweel J (2008) The EUROPIV synthetic image generator. Technical report
Lewis JP (1995) Fast normalized cross-correlation. Vision interface
Maas H, Gruen A, Papantoniou D (2004) Particle tracking velocimetry in three-dimensional flows. Exp Fluids 15:133–146
Matzle C (2002) MATLAB functions for mie scattering and absorption. Technical report. Institute of Applied Physics, University of Bern
Overmars EFJ, Warncke NGW, Poelma C, Westerweel J (2010) Bias errors in piv: the pixel locking effect revisited. In: Proceedings of the 15th international symposium on applications of laser techniques to fluid mechanics
Phong BT (1975) Illumination for computer generated pictures. Commun ACM 18:311–317
Scarano F (2001) Iterative image deformation methods in PIV. Meas Sci Technol 13:R1–R19
Scarano F, Poelma C (2009) Three-dimensional vorticity patterns of cylinder wakes. Exp Fluids 47:69–83
Tropea C, Yarin AL, Foss JF (2007) Springer handbook of experimental fluid mechanics. Springer, New York
Westerweel J (1997) Fundamentals of digital particle image velocimetry. Meas Sci Technol 8:1379–1392
Westerweel J (2000) Theoretical analysis of the measurement precision in particle image velocimetry. Exp Fluids 29:S3–S12
Willert CE, Gharib M (1991) Digital particle image velocimetry. Exp Fluids 10:181–193
Worth NA, Nickels TB (2008) Acceleration of Tomo-PIV by estimating the initial volume intensity distribution. Exp Fluids 45:847–856
Worth NA, Nickels TB, Swaminathan N (2010) A tomographic PIV resolution study based on homogeneous isotropic turbulence DNS data. Exp Fluids 49:637–656